

Quantum and Thermal Phase Transitions of the Triangular SU(3) Heisenberg Model under Magnetic Fields

Daisuke Yamamoto, Chihiro Suzuki, Giacomo Marmorini, Sho Okazaki, and Nobuo Furukawa

Department of Physics and Mathematics, Aoyama Gakuin University, Sagamihara, Kanagawa 252-5258, Japan

(Dated: September 11, 2022)

We study the quantum and thermal phase transition phenomena of the SU(3) Heisenberg model on triangular lattice in the presence of magnetic fields. Performing a scaling analysis on large-size cluster mean-field calculations endowed with a density-matrix-renormalization-group solver, we reveal the quantum phases selected by quantum fluctuations from the massively degenerate classical ground-state manifold. The magnetization process up to saturation reflects three different magnetic phases. The low- and high-field phases have strong nematic nature, and especially the latter is found only via a nontrivial reconstruction of symmetry generators from the standard spin and quadrupolar description. We also perform a semi-classical Monte-Carlo simulations to show that thermal fluctuations prefer the same three phases as well. Moreover, we find that exotic topological phase transitions driven by the binding-unbinding of fractional (half) vortices take place, due to the nematicity of the low- and high-field phases. Possible experimental realization with alkaline-earth-like cold atoms is also discussed.

Introduction.— In solid-state physics, lattice Hamiltonians symmetric under the special unitary group of degree $\mathcal{N} = 2$, denoted by SU(2), have been intensively studied since the electron – the main actor in solids – has two internal (spin) degrees of freedom. Higher degree of symmetry, or $\mathcal{N} > 2$, can be accessed only with fine-tuning of parameters in some models, e.g., of spin liquid crystals [1–3] and transition metal oxides [4–7], or as a consequence of exotic emergent phases [8–10]. However, recent advances in experiments with cold gases of alkaline-earth(-like) atoms, such as ^{173}Yb [11–16] and ^{87}Sr [17, 18], have provided a new platform and strong motivation in studying the enhanced continuous symmetry of $\text{SU}(\mathcal{N} > 2)$. Since those atoms possess symmetric interactions under nuclear spin \mathbf{I} ($I = 5/2$ for Yb and $9/2$ for Sr), loading them into optical lattices enables us to create an ideal quantum simulator of the $\text{SU}(\mathcal{N} \leq 2I+1)$ extension of the Hubbard model [19] and its strong-coupling limit, namely the $\text{SU}(\mathcal{N})$ Heisenberg model [20, 21]. In such higher symmetric systems, the ground states often form a massively (quasi-)degenerate manifold. Therefore, of particular interest are the quantum and thermal fluctuations selecting one of the many-body states and the emergence of exotic phase transition phenomena [23].

The SU(3) Heisenberg model on triangular lattice has been theoretically studied as a special symmetric point of the spin-1 bilinear-biquadratic (BLBQ) model [24–26]. Since the number of colors ($\mathcal{N} = 3$) is compatible with the tripartite structure of the triangular lattice, the SU(3) Heisenberg model with antiferromagnetic couplings exhibits no (apparent) geometrical frustration, unlike the SU(2) case [27]. Indeed, the ground state is uniquely determined (up to trivial degeneracy) to be a simple three-color three-sublattice order at the level of the classical, mean-field (MF), analysis [24, 25], and it has been confirmed by numerical investigations [26].

Whereas the ground state may not be so exciting, the properties under the presence of magnetic field remain an interesting open problem since the MF analysis yields an accidental continuous degeneracy [24]. It is thus required to study the degeneracy lifting induced by quantum and thermal fluctuations.

In this work, we explore the effect of quantum and thermal fluctuations on the phase transition phenomena of the triangular SU(3) Heisenberg model in magnetic fields. High magnetic field experiments have been playing a central role in understanding the properties of magnetic materials [28], one of the fundamental reasons being that a magnetic field, in combination with lattice geometry, topological features, fluctuation effects, etc., stimulates the emergence of a rich variety of nontrivial magnetic states such as magnetization plateaus [29–31], nematic states [32, 33], and field-induced quantum spin liquids [31, 34]. This is naturally expected to occur for general $\text{SU}(\mathcal{N})$ systems. In experiments with \mathcal{N} -color components of cold atoms, the “magnetic field” in the sense of spin models could be implemented by introducing a difference among the chemical potentials for different color components. The recent quantum simulation of the SU(2) Heisenberg model has demonstrated that the magnetic-field effect can indeed be obtained by introducing finite population imbalance between the two hyperfine states of ^6Li [35].

First, we employ the cluster mean-field plus scaling (CMF+S) method [36–38] with two-dimensional (2D) density matrix renormalization group (DMRG) solver [39] to reveal the quantum phases selected from the nontrivial classical ground-state manifold. We find that the quantum order-by-disorder mechanism stabilizes three different phases with the three-sublattice structure depending on the field strength, until the system reaches the magnetic saturation. Of particular interest is the low-field phase, whose field-dependence exhibits nontriv-

ial preservation of the uniform (total) scalar nematic order parameter at zero value, despite of having a finite value on each sublattice. In addition, the intermediate-field phase also preserves the total magnetization as well, resulting in a characteristic plateau structure in the magnetization curve at $2/3$ of the saturation magnetization. Even more interestingly, although the high-field phase appears to be a conventional (non-nematic) spin order in terms of the spin and quadrupolar operators, we reveal a concealed nematic nature by performing a unitary transformation to reconstruct the symmetry generators. Furthermore, we develop a framework of *semi-classical* multi-color Monte-Carlo (sMC) simulations [40] by introducing a “relaxation acceleration” technique, and discuss the thermal phase transition phenomena. In addition to the stabilization of the same three phases by thermal fluctuations, we find particular topological phase transitions characterized by the binding-unbinding of fractional (half) vortices.

The $SU(3)$ Heisenberg model in magnetic fields.— The $SU(3)$ Heisenberg model is given by

$$\hat{\mathcal{H}}_{SU(3)} = 2J \sum_{\langle i,j \rangle} \sum_{A=1,2,\dots,8} \hat{T}_i^A \hat{T}_j^A \quad (J > 0), \quad (1)$$

where $\hat{T}_i^A = \hat{\lambda}_i^A/2$ are the eight generators of the $SU(3)$ Lie algebra in the defining representation. To draw connections to the spin physics, here we employ the spin-1 operator $\hat{\mathbf{S}}_i = (\hat{S}_i^x, \hat{S}_i^y, \hat{S}_i^z)$ for $A = 1, 2, 3$ and the quadrupolar operator $\hat{\mathbf{Q}}_i = (\hat{Q}_i^{x^2-y^2}, \hat{Q}_i^{z^2}, \hat{Q}_i^{xy}, \hat{Q}_i^{yz}, \hat{Q}_i^{xz})$ for $A = 4, \dots, 8$ as $\hat{\lambda}_i^A$, instead of the standard Gell-Mann matrix basis. The quadrupolar operators are $(\hat{S}_i^x)^2 - (\hat{S}_i^y)^2, \sqrt{3}(\hat{S}_i^z)^2 - 2/\sqrt{3}, \hat{S}_i^x \hat{S}_i^y + \hat{S}_i^y \hat{S}_i^x, \hat{S}_i^y \hat{S}_i^z + \hat{S}_i^z \hat{S}_i^y$, and $\hat{S}_i^z \hat{S}_i^x + \hat{S}_i^x \hat{S}_i^z$, respectively. In this spin-1 representation, the Hamiltonian (1) is equivalent to the BLBQ model [23–26, 41, 42] with equal positive coefficients, acting on spin states $\sigma = -1, 0, 1$:

$$\hat{\mathcal{H}}_{SU(3)} = \frac{J}{2} \sum_{\langle i,j \rangle} \left(\hat{\mathbf{S}}_i \cdot \hat{\mathbf{S}}_j + \hat{\mathbf{Q}}_i \cdot \hat{\mathbf{Q}}_j \right). \quad (2)$$

Below, we discuss the system under magnetic (Zee-man) fields: $\hat{\mathcal{H}} \equiv \hat{\mathcal{H}}_{SU(3)} + \hat{\mathcal{H}}_Z$ with $\hat{\mathcal{H}}_Z = -H \sum_i \hat{S}_i^z$. The magnetic field explicitly breaks the $SU(3)$ symmetry down to $U(1) \times U(1)$; specifically, the global rotations around the \hat{S}^z and \hat{Q}^{z^2} axes remain since $\sum_i [\hat{S}_i^z, \hat{\mathcal{H}}] = \sum_i [\hat{Q}_i^{z^2}, \hat{\mathcal{H}}] = 0$. Hereafter, we specifically write the two rotational symmetries as $U(1)_{S^z}$ and $U(1)_{Q^{z^2}}$. Within the site-decoupling MF approximation [24], the specific spin and quadratic orders in the ground state for $0 < H < H_s$ (with $H_s = 9J$) exhibit a massive, accidental degeneracy not related to the symmetries of the system. The detailed structure of the degenerate ground-state manifold is described in the Supplementary Material (SM).

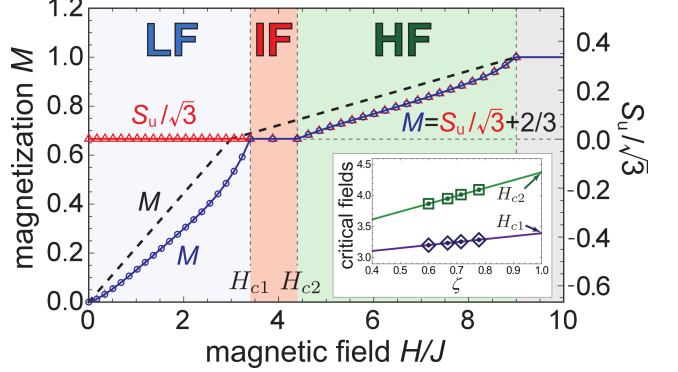


FIG. 1: Field dependences of the magnetization M (blue circles) and the uniform scalar nematic order parameter S_u (devided by $\sqrt{3}$; red triangles), obtained by the CMF+S analysis. The MF value of M is plotted together (dashed line). Left and right axes are shifted by $2/3$. The inset shows cluster-size scalings of the critical fields.

Quantum order-by-disorder.— In order to discuss the lifting of the accidental degeneracy by quantum fluctuations and reveal the quantum orders, we perform the CMF+S calculations [36–38] with 2D DMRG solver [39]. We employ a triangular-shaped cluster of N_C sites, in which the quantum intersite correlations are treated exactly within the cluster, whereas the couplings with the outside spins are replaced by MF interactions. Under the three-sublattice ($\mu = A, B, C$) ansatz, the self-consistent equations $\langle \hat{\mathbf{S}}_\mu \rangle = \frac{3}{N_C} \sum_{i_\mu \in C} \langle \Psi_{N_C} | \hat{\mathbf{S}}_{i_\mu} | \Psi_{N_C} \rangle$ and the analogous expressions for $\langle \hat{\mathbf{Q}}_\mu \rangle$ are solved by calculating the ground state of the N_C -site cluster, $|\Psi_{N_C}\rangle$, with 2D DMRG in an iterative way until convergence [39]. The scaling parameter $\zeta \equiv N_B/(3N_C)$, with N_B being the number of bonds inside the cluster, serves as an indicator of the extent to which quantum correlations are taken into account, interpolating the classical (MF; $\zeta = 0$) and exactly-quantum ($N_C \rightarrow \infty$; $\zeta = 1$) limits. Here we perform the calculations for $N_C = 10, 15, 21$ ($\zeta = 3/5, 2/3, 5/7$) and make the linear extrapolation of the results towards $\zeta \rightarrow 1$ with an error bar estimated from the derivation of different sets of cluster sizes used for the extrapolation. The larger size cluster of $N_C = 36$ ($\zeta = 7/9$) is also considered for the determination of the phase boundaries (see the inset of Fig. 1).

We plot the quantum magnetization curves $M(H) \equiv \sum_\mu \langle \hat{S}_\mu^z \rangle / 3$ obtained by the CMF+S in Fig. 1, which shows three different phases separated by the critical fields $H_{c1} = 3.40$ and $H_{c2} = 4.38$ in the range of $0 < H < H_s$. The low-field (LF) phase is characterized by $\langle \hat{S}_A^z \rangle = \langle \hat{S}_B^z \rangle \neq \langle \hat{S}_C^z \rangle \approx 0$, $\langle \hat{Q}_A^{x^2-y^2} \rangle = -\langle \hat{Q}_B^{x^2-y^2} \rangle$, and $\langle \hat{Q}_C^{x^2-y^2} \rangle = 0$, modulo a global rotation in the $(Q^{x^2-y^2}, Q^{xy})$ plane and sublattice exchanges; the other components are all zero [see Fig. 2(a)]. Although the spin sector (S^x, S^y, S^z) forms a collinear structure along the field

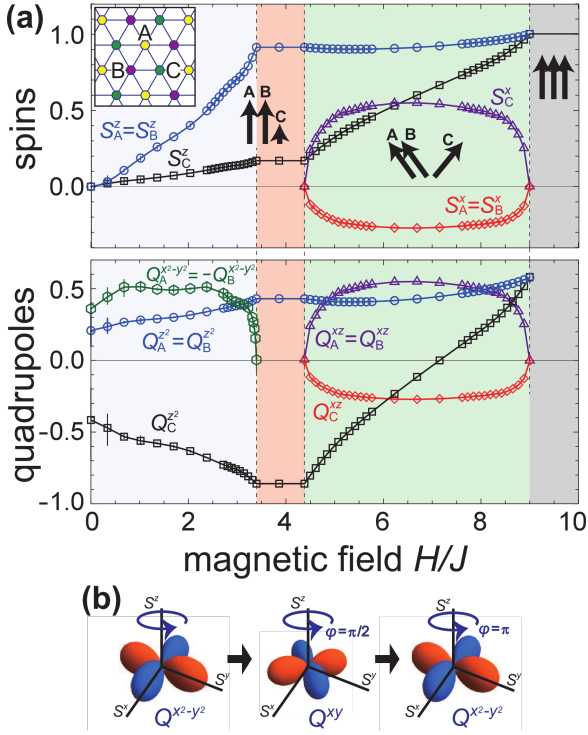


FIG. 2: (a) Nonzero components of the spin and quadrupolar moments, obtained by the CMF+S analysis in a fixed gauge with $\langle \hat{Q}_A^{xy} \rangle = \langle \hat{Q}_A^{yz} \rangle = 0$. The inset shows the three-sublattice structure. (b) Spherical plots of $|\langle \mathbf{S} | \hat{Q}^{x^2-y^2} | \mathbf{S} \rangle|$ and its $\pi/2$ and π rotations about $U(1)_{S^z}$ with $|\mathbf{S}\rangle$ being the spin coherent state pointing in the \mathbf{S} direction [23].

axis, the transverse quadrupolar moments ($Q^{x^2-y^2}$, Q^{xy}) break the rotational symmetry around S^z . It is particularly interesting that the a π -rotation around the S^z axis is sufficient for $(Q^{x^2-y^2}, Q^{xy})$ to return the initial state as illustrated in Fig. 2(b) due to the nematic nature, reflecting the factor 2 in the commutation relation $[\hat{Q}^{x^2-y^2}, \hat{Q}^{xy}] = 2i\hat{S}^z$. Thus, it is concluded that the LF phase breaks the $(U(1)_{S^z}/\mathbb{Z}_2) \times \mathbb{Z}_3$ (i.e., half of the original rotational and three-fold translational) symmetries. Consequently, the remaining $U(1)_{Q^{z^2}}$ symmetry guarantees the preservation of the uniform nematic scalar order parameter $S_u \equiv \sum_\mu \langle \hat{Q}_\mu^{z^2} \rangle / 3$, resulting in the plateau formation at zero value in the field dependence (Fig. 1), whereas each sublattice value $\langle \hat{Q}_\mu^{z^2} \rangle$ is finite [Fig. 2(a)].

At $H = H_{c1}$, the transverse quadrupolar moments vanish and the $U(1)_{S^z}$ symmetry is restored. Thus, in the intermediate-field (IF) phase, both M and S_u exhibit plateau behavior in the range of $H_{c1} < H < H_{c2}$. The longitudinal spin moments $\langle \hat{S}_\mu^z \rangle$ have the values of approximately $(1, 1, 0)$ (not exactly, due to quantum depletion) and thus $M = 2/3$. Such a plateau formation has been reported in the spin-1 BLBQ model when the quadrupolar coupling is larger than the dipolar one [24]. Our results showed that the plateau is stabi-

lized by purely quantum effects even for equal bilinear-biquadratic ($SU(3)$ -symmetric) coupling.

In the high-field (HF) phase, the spin (S^x, S^y, S^z) sector forms a “2:1” structure of the V shape, similar to the $SU(2)$ case [29]. Therefore, it apparently seems to be a standard non-nematic spin order. However, we notice that the curves of M and $S_u/\sqrt{3}$ differ only by a constant shift of $2/3$. We show that this feature stems from a particular spontaneous partial breaking of $U(1)_{S^z} \times U(1)_{Q^{z^2}}$: the linear combination of generators $\hat{P}_+^z \equiv \frac{1}{2}\hat{S}^z + \frac{\sqrt{3}}{2}\hat{Q}^z$ is broken, while $\hat{P}_-^z \equiv \frac{\sqrt{3}}{2}\hat{S}^z - \frac{1}{2}\hat{Q}^z$ is preserved. The $U(1)_{P_\pm^z}$ action produces a rotation of the system in the plane of $\hat{P}_\pm^x \equiv (\hat{S}^x \pm \hat{Q}^{xz})/\sqrt{2}$ and $\hat{P}_\pm^y \equiv (\hat{S}^y \pm \hat{Q}^{yz})/\sqrt{2}$. As is seen in Fig. 2(a), the transverse spin and quadrupolar moments hold the relation $\langle \hat{P}_{\pm, \mu}^x \rangle = \langle \hat{P}_{\pm, \mu}^y \rangle = 0$ in the HF phase, which indicates the preservation of the $U(1)_{P_\pm^z}$ symmetry. As for the broken $U(1)_{P_+^z}$, a π -rotation is sufficient for $(\hat{P}_+^x, \hat{P}_+^y)$ to return to the initial state since $[\hat{P}_+^x, \hat{P}_+^y] = 2i\hat{P}_+^z$, and thus the HF phase possesses a nematic nature despite of the apparent spin (dipolar) order. Considering also the sublattice exchange, we conclude that the HF phase breaks $(U(1)_{P_+^z}/\mathbb{Z}_2) \times \mathbb{Z}_3$.

Thermal phase diagram.— Given the strong nematic nature of the zero-temperature phases, it is interesting to study the thermal phase transitions, especially associated with the $(U(1)/\mathbb{Z}_2) \times \mathbb{Z}_3$ symmetry breaking. To this end, we employ the sMC simulations [40] within the direct-product approximation: $|\Psi^{\text{cl}}\rangle = \otimes_i |\psi_i\rangle$ with local wave functions $|\psi_i\rangle = \sum_{\sigma} d_{i,\sigma} |\sigma_i\rangle$ ($|d_i|^2 = 1$). The standard Metropolis updates are performed for the coefficients $d_{i,\sigma}$ on $L \times L$ rhombic clusters under periodic boundary conditions, based on the Boltzmann distribution $p \propto \exp(-E_{\text{cl}}/k_B T)$ with $E_{\text{cl}} \equiv \langle \Psi^{\text{cl}} | \hat{\mathcal{H}} | \Psi^{\text{cl}} \rangle$ [40]. We further develop the sMC method by applying a “relaxation acceleration” (RA) with local unitary transformations $e^{ic\hat{\mathcal{H}}_i^{\text{loc}}} |\psi_i\rangle$, where c are uniformly distributed random numbers and $\hat{\mathcal{H}}_i^{\text{loc}} \equiv (\otimes_{j \neq i} \langle \psi_j |) \hat{\mathcal{H}} (\otimes_{j \neq i} | \psi_j \rangle)$. Here we choose, after some trials, $|c| \leq \pi \|\hat{\mathcal{H}}_i^{\text{loc}}\|_{\text{F}}$ with $\|\cdots\|_{\text{F}}$ being the Frobenius norm. The RA sweeps over lattice sites are performed twice following each Metropolis update sweep. This method, applied to highly-symmetric systems, is significantly more efficient in improving decorrelation and avoiding trapping in local minima. See the SM [43] for more technical details and the performance examination of the RA procedure.

Figure 3 shows the thermal phase diagram obtained by the sMC, which is reliable in the region away from the low-temperature quantum regime, since it neglects the inter-site quantum correlations. It is seen that the same three (LF, IF, and HF) phases are selected also by thermal fluctuations from the classical degenerate manifolds at $T = 0$. The boundaries to the paramagnetic phase are determined from the divergence of the correlation length of the longitudinal (S^z, Q^{z^2} ; indicated by square sym-

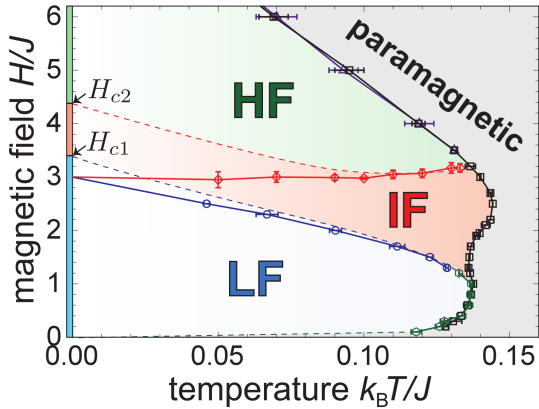


FIG. 3: Thermal phase diagram obtained by the sMC simulations. We also mark the critical fields H_{c1} and H_{c2} obtained by the CMF+S method at the quantum ($T = 0$) limit. The dashed lines are the sketches of the phase boundaries expected from the combination of the sMC (valid at high temperatures) and CMF+S (valid at $T = 0$) results.

bols) and transverse (all the others; indicated by triangles and hexagons) components of the three-sublattice order parameters. The LF-IF and IF-HF boundaries are determined by the scaling analyses of the susceptibility in the corresponding transverse components.

We show in Fig. 4(a) the stiffness $\rho_{S^z}(T)$ for a twist of the spin and quadrupolar moments around S^z in the transition region between LF and IF. It can be clearly seen that $\rho_{S^z}(T)$ at the transition point $T = T_c$ does not satisfy the standard universal relation $\rho_{S^z}(T_c) = 2k_B T_c / \pi$ for the Kosterlitz-Thouless (KT) transitions [44]. This is attributed to the nematic nature of $(Q^{x^2-y^2}, Q^{xy})$, which break $U(1)/\mathbb{Z}_2$ rotations around S^z [shown in Fig. 2(b)]. Due to this, the $(Q^{x^2-y^2}, Q^{xy})$ moments can form a topologically stable vortex with fractional vorticity $\rho_v = 1/2$ [Fig. 4(b)], unlike in the standard XY universality class, where $\rho_v = 1$. This half-vortex is analogous to the 180 degree disclination of nematic liquid crystals [45]. The transition from LF to IF is associated with the unbinding of pairs of half-vortex and half-antivortex, resulting in the modified universal relation $\rho_{S^z}(T_c) = 2k_B T_c / \pi \rho_v^2 = 8k_B T_c / \pi$ [46]. This particular topological transition takes place also at the boundary of the HF and IF (or paramagnetic) phase [Fig. 4(c)], where it is related to the $U(1)/\mathbb{Z}_2$ rotation around P_+^z mentioned above. This universal jump is associated with the unbinding of half-vortex pairs in the (P_+^x, P_+^y) plane. Note that we confirmed that the stiffness for a twist around P_-^z is always zero (within the numerical error) in the HF phase.

Let us comment briefly on the limit of zero magnetic field. Since the classical ground state is given by $\mathbf{d}_i = (1, 0, 0)$, $(0, 1, 0)$, and $(0, 0, 1)$ for sublattice A, B, and C, respectively, or $SU(3)$ rotations thereof [25], the symmetry is spontaneously broken down to $U(1) \times U(1)$.

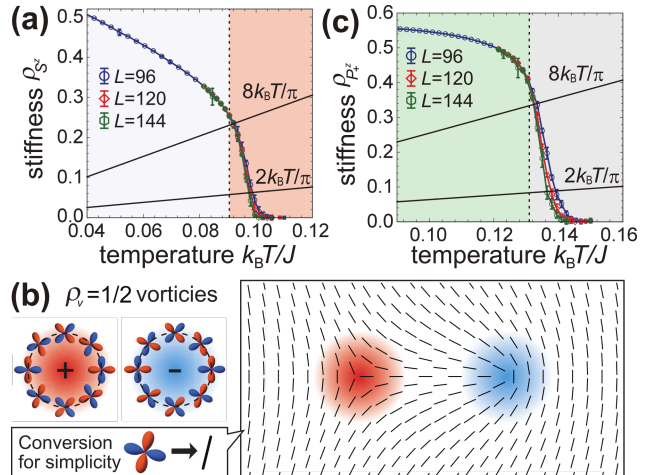


FIG. 4: (a) Stiffness $\rho_{S^z}(T)$ along $H/J = 2.0$, which shows a universal jump $\rho_{S^z}(T_c) = 8k_B T_c / \pi$ at the LF-IF transition, except for a slight finite-size effect. (b) Vortex and antivortex with half vorticity $\rho_v = \pm 1/2$ in the projected $(Q^{x^2-y^2}, Q^{xy})$ plane. The right panel is a schematic illustration of a topological half-vortex pair excitation on the background of a uniform quadrupolar order on, say, sublattice A. (c) Same as in (a) for $\rho_{P_+^z}(T)$ at the HF-paramagnetic transition along $H/J = 3.5$.

The fundamental group $\pi_1(SU(3)/U(1) \times U(1))$ is trivial [47] and therefore there are no vortex-induced finite temperature phase transitions [44, 48]. The tendency of the IF-paramagnetic line towards the $(T, H) = (0, 0)$ point corroborates this scenario.

Experimental realization.— In optical-lattice experiments with alkaline-earth(-like) atoms, the field strength H corresponds to the difference in the chemical potentials of each component: $\mu_1 - \mu_0 = \mu_0 - \mu_{-1} = H$. This could be prepared via the population imbalance in different colors [35]. More directly, if one could introduce a state-dependent gradient potential, say, in the x direction, $V_\sigma^{\text{ext}}(x) = \sigma V x$, the magnetization process in $-H_s < H < H_s$ would be realized as the spatial dependence for local magnetic field $H(x) = 2Vx$ (in the sense of the local density approximation [49]) with no overall population imbalance. The formation of the three-sublattice orders can be detected by the time-of-flight image of the momentum distribution [35, 50–54], and the IF state would appear as a spatial plateau. In addition, the extension of the quantum-gas microscope technique to $SU(N)$ systems could provide a wealth of detailed measurements of each phase found here.

Conclusions.— We studied the quantum and thermal phase transition phenomena of the $SU(3)$ Heisenberg model under magnetic fields by using the CMF+S and sMC methods. We demonstrated that pure quantum-fluctuation effects stabilize a magnetization plateau at $2/3$ of the saturation in the intermediate range of the field strength. The uniform scalar nematic order parameter also forms a plateau at zero value, which, more inter-

estingly, appears already in the lower-field phase with no magnetization plateau. This reflects the preservation of additional $U(1)$ symmetry around Q^z unique to the system with the $SU(3)$ symmetry (reduced to $U(1) \times U(1)$ under magnetic fields). The high-field phase exhibits an unexpected nematic nature stemming from nontrivial partial breaking of $U(1) \times U(1)$ symmetry. Moreover, the strong nematic nature of the low- and high-field phases gives rise to fractional vortices and antivortices, whose pair dissociation results in a topological phase transition with vorticity $\rho_v = 1/2$ at the critical temperature.

The above results, together with the calculated critical temperatures ($\approx 0.14J/k_B$ at the highest value), provide a solid guideline for future experiments with alkaline-earth(-like) atoms. Besides, the physics we explored is relevant to solid-state materials with nearly $SU(3)$ symmetric parameters and, more generally, to systems with multipolar orders. Finally, it should be mentioned that the calculation methods used here can be applied to numerous types of classical and quantum simulations; especially, the acceleration and decorrelation of the sMC updates by the RA technique are expected to become increasingly important for models with higher symmetry, such as $SU(N \geq 3)$.

We thank Y. Takahashi and I. Danshita for valuable discussions on this subject. This work was supported by KAKENHI from Japan Society for the Promotion of Science: Grant Numbers 18K03525 (D.Y.), CREST from Japan Science and Technology Agency No. JPMJCR1673 (D.Y.), and “Early Eagle” grant program from Aoyama Gakuin University Research Institute.

[1] S. Nakatsuji, Y. Nambu, H. Tonomura, O. Sakai, S. Jonas, C. Broholm, H. Tsunetsugu, Y. Qiu, and Y. Maeno, *Science* **309**, 1697 (2005).

[2] H. Tsunetsugu and M. Arikawa, *J. Phys. Soc. Jpn.* **75**, 083701 (2006).

[3] S. Bhattacharjee, V. B. Shenoy and T. Senthil, *Phys. Rev. B* **74**, 092406 (2006).

[4] K. I. Kugel and D. I. Khomskii, *Sov. Phys. JETP* **37**, 725 (1973).

[5] D. P. Arovas and A. Auerbach, *Phys. Rev. B* **52**, 10114 (1995).

[6] Y. Q. Li, M. Ma, D. N. Shi, and F. C. Zhang, *Phys. Rev. Lett.* **81**, 3527 (1998).

[7] Y. Tokura and N. Nagaosa, *Science* **288**, 462 (2000).

[8] A. J. Keller, S. Amasha, I. Weymann, C. P. Moca, I. G. Rau, J. A. Katine, H. Shtrikman, G. Zarand, and D. Goldhaber-Gordon, *Nature Physics* **10**, 145 (2014).

[9] P. Chen, Z.-L. Xue, I. P. McCulloch, M.-C. Chung, C.-C. Huang, and S.-K. Yip, *Phys. Rev. Lett.* **114**, 145301 (2015).

[10] V. L. Quito, Pedro L. S. Lopes, Jose A. Hoyos, E. Miranda, *Eur. Phys. J. B* **93**, 17 (2020).

[11] T. Fukuhara, Y. Takasu, M. Kumakura, and Y. Takahashi, *Phys. Rev. Lett.* **98**, 030401 (2007).

[12] M. A. Cazalilla, A. F. Ho, and M. Ueda, *New J. Phys.* **11**, 103033 (2009).

[13] H. Hara, Y. Takasu, Y. Yamaoka, J. M. Doyle, and Y. Takahashi, *Phys. Rev. Lett.* **106**, 205304 (2011).

[14] S. Taie, R. Yamazaki, S. Sugawa, and Y. Takahashi, *Nat. Phys.* **8**, 825 (2012).

[15] C. Hofrichter, L. Rieger, F. Scazza, M. Höfer, D. R. Fernandes, I. Bloch, and S. Fölling, *Phys. Rev. X* **6**, 021030 (2016).

[16] H. Ozawa, S. Taie, Y. Takasu, and Y. Takahashi, *Phys. Rev. Lett.* **121**, 225303 (2018).

[17] B. J. DeSalvo, M. Yan, P. G. Mickelson, Y. N. Martinez de Escobar, and T. C. Killian, *Phys. Rev. Lett.* **105**, 030402 (2010).

[18] M. K. Tey, S. Stellmer, R. Grimm, and F. Schreck, *Phys. Rev. A* **82**, 011608(R) (2010).

[19] C. Honerkamp and W. Hofstetter, *Phys. Rev. Lett.* **92**, 170403 (2004).

[20] A. V. Gorshkov, M. Hermele, V. Gurarie, C. Xu, P. S. Julienne, J. Ye, P. Zoller, E. Demler, M. D. Lukin, and A. M. Rey, *Nat. Phys.* **6**, 289 (2010).

[21] P. Nataf and F. Mila, *Phys. Rev. Lett.* **113**, 127204 (2014).

[22] J. S. Gardner, M. J. P. Gingras, and J. E. Greedan, *Rev. Mod. Phys.* **82**, 53 (2010).

[23] *Introduction to Frustrated Magnetism*, edited by C. Lacroix, P. Mendels, and F. Mila (Springer-Verlag, Berlin, 2011).

[24] A. Läuchli, F. Mila, and K. Penc, *Phys. Rev. Lett.* **97**, 087205 (2006).

[25] A. Smerald and N. Shannon, *Phys. Rev. B* **88**, 184430 (2013).

[26] B. Bauer, P. Corboz, A. M. Läuchli, L. Messio, K. Penc, M. Troyer, F. Mila, *Phys. Rev. B* **85**, 125116 (2012).

[27] R. Moessner and A. P. Ramirez, *Physics Today* **59**, 24 (2006).

[28] *High Magnetic Fields: Applications in Condensed Matter Physics and Spectroscopy*, edited by C. Berthier, L.-P. Levy, and G. Martinez (Springer-Verlag, Berlin, 2002).

[29] A. V. Chubukov and D. I. Golosov, *J. Phys.: Condens. Matter* **3**, 69 (1991).

[30] Y. Shirata, H. Tanaka, A. Matsuo, and K. Kindo, *Phys. Rev. Lett.* **108**, 057205 (2012).

[31] S. Nishimoto, N. Shibata, and C. Hotta, *Nat. Commun.* **4**, 2287 (2013).

[32] K. Nawa, M. Takigawa, M. Yoshida, and K. Yoshimura, *J. Phys. Soc. Jpn.* **82**, 094709 (2013).

[33] N. Büttgen, K. Nawa, T. Fujita, M. Hagiwara, P. Kuhns, A. Prokofiev, A. P. Reyes, L. E. Svistov, K. Yoshimura, and M. Takigawa, *Phys. Rev. B* **90**, 134401 (2014).

[34] S.-H. Baek, S.-H. Do, K.-Y. Choi, Y. S. Kwon, A. U. B. Wolter, S. Nishimoto, J. van den Brink, and B. Büchner, *Phys. Rev. Lett.* **119**, 037201 (2017).

[35] P. T. Brown, D. Mitra, E. Guardado-Sánchez, P. Schauß, S. S. Kondov, E. Khatami, T. Paiva, N. Trivedi, D. A. Huse, W. S. Bakr, *Science* **357**, 1385 (2017).

[36] D. Yamamoto, A. Masaki, and I. Danshita, *Phys. Rev. B* **86**, 054516 (2012).

[37] D. Yamamoto, G. Marmorini, and I. Danshita, *Phys. Rev. Lett.* **112**, 127203 (2014); *ibid.* **112**, 259901 (2014).

[38] D. Yamamoto, H. Ueda, I. Danshita, G. Marmorini, T. Momoi, and T. Shimokawa, *Phys. Rev. B* **96**, 014431 (2017).

[39] D. Yamamoto, G. Marmorini, M. Tabata, K. Sakakura,

and I. Danshita, Phys. Rev. B **100**, 140410(R) (2019).

[40] E. M. Stoudenmire, S. Trebst, and L. Balents, Phys. Rev. B **79**, 214436 (2009).

[41] T. A. Toth, A. M. Läuchli, F. Mila, K. Penc, Phys. Rev. B **85**, 140403(R) (2012).

[42] I. Niesen and P. Corboz, Phys. Rev. B **95**, 180404(R) (2017); *ibid.* **97**, 245146 (2018).

[43] See Supplemental Material at [http://\[URL\]](http://[URL]) for detailed structure of the degenerate classical ground-state manifold and technical details of the sMC simulations.

[44] J. M. Kosterlitz, Rep. Prog. Phys. **79**, 026001 (2016).

[45] N. D. Mermin, Rev. Mod. Phys. **51**, 591 (1979).

[46] S. E. Korshunov Phys. Rev. B **65**, 054416 (2002).

[47] H. T. Ueda, Y. Akagi, and N. Shannon, Phys. Rev. A **93**, 021606(R) (2016).

[48] H. Kawamura and S. Miyashita, J. Phys. Soc. Jpn. **53**, 4138 (1984); H. Kawamura, A. Yamamoto, and T. Okubo, J. Phys. Soc. Jpn. **79**, 023701 (2010).

[49] S. Bergkvist, P. Henelius, and A. Rosengren, Phys. Rev. A **70**, 053601 (2004).

[50] M. F. Parsons, A. Mazurenko, C. S. Chiu, G. Ji, D. Greif, and M. Greiner, Science **353**, 1253 (2016).

[51] M. Boll, T. A. Hilker, G. Salomon, A. Omran, J. Nespolo, L. Pollet, I. Bloch, and C. Gross, Science **353**, 1257 (2016).

[52] L. W. Cheuk, M. A. Nichols, K. R. Lawrence, M. Okan, H. Zhang, E. Khatami, N. Trivedi, T. Paiva, M. Rigol, and M. W. Zwierlein, Science **353**, 1260 (2016).

[53] A. Mazurenko, C. S. Chiu, G. Ji, M. F. Parsons, M. Kanász-Nagy, R. Schmidt, F. Grusdt, E. Demler, D. Greif, and M. Greiner, Nature (London) **545**, 462 (2017).

[54] T. A. Hilker, G. Salomon, F. Grusdt, A. Omran, M. Boll, E. Demler, I. Bloch, and C. Gross, Science **357**, 484 (2017).

Supplementary Material for “Quantum and Thermal Phase Transitions of the Triangular SU(3) Heisenberg Model under Magnetic Fields”

Classical degeneracy manifold of the triangular SU(3) Heisenberg model with magnetic fields

Within the site-decoupling mean-field (MF) approximation, the ground state is assumed to be a direct product of local wave-functions ($|\mathbf{d}_i|^2 = 1$):

$$|\Psi^{\text{cl}}\rangle = \otimes_i |\psi_i\rangle \quad \text{with} \quad |\psi_i\rangle = \sum_{\sigma} d_{i,\sigma} |\sigma_i\rangle. \quad (\text{S1})$$

The coefficient vector $\mathbf{d}_i = (d_{i,-1}, d_{i,0}, d_{i,1})$ normalized to unit length ($|\mathbf{d}_i| = 1$) identifies the local state at site i as a superposition of the three basis states ($\sigma = -1, 0, 1$). Under the three-sublattice ($\mu = \text{A}, \text{B}, \text{C}$) ansatz, the variational energy $E_{\text{cl}} \equiv \langle \Psi^{\text{cl}} | \hat{\mathcal{H}} | \Psi^{\text{cl}} \rangle$ can be written as

$$\frac{E_{\text{cl}}}{N} = \frac{J}{4} \left(\boldsymbol{\lambda}_{\text{A}} + \boldsymbol{\lambda}_{\text{B}} + \boldsymbol{\lambda}_{\text{C}} - \frac{2\mathbf{H}}{3J} \right)^2 - \frac{h^2}{9J} - J, \quad (\text{S2})$$

where N is the number of sites, $\boldsymbol{\lambda}_{\mu} \equiv \langle \Psi^{\text{cl}} | \hat{\lambda}_{i,\mu} | \Psi^{\text{cl}} \rangle$ is an eight-component classical vector of length $\sqrt{4/3}$, and $\mathbf{H} = (0, 0, H, 0, 0, 0, 0, 0)$. The minimization of E_{cl} is simply achieved when $\overline{\boldsymbol{\lambda}_{\mu}} = 2\mathbf{H}/9J$ for $h \leq 3J$. The overline means the average over $\mu = \text{A}, \text{B}, \text{C}$. For $H > 3J$, the two conditions $\overline{S_{\mu}^z} = 2H/9J$ and $\overline{Q_{\mu}^{z^2}} = 0$, cannot be simultaneously satisfied because $Q_{\mu}^{z^2}/\sqrt{3}$ must be larger than $S_{\mu}^z - 2/3$ from the definition. After some algebra, we found the conditions $\overline{S_{\mu}^z} = H/6J + 3/2$ and $\overline{Q_{\mu}^{z^2}} = H/4J - 3/4$ in the range of $3J < H < H_s$, with $H_s = 9J$ being the saturation field.

From the above discussion, the magnetization $M \equiv \sum_i \langle \hat{S}_i^z \rangle / N = \overline{S_{\mu}^z}$ is uniquely determined as shown in Fig. 1 (dashed line). However, the specific spin and quadratic orders remain massively degenerate because the number of conditions is smaller than that of variational parameters $d_{i,\mu,\sigma}$.

Technical details of the semi-classical Monte Carlo analysis

In the main text, we employ the semi-classical Monte Carlo (sMC) simulations [1] on $L \times L$ rhombic clusters under periodic boundary conditions, since the fully-quantum Monte Carlo method suffers from the so-called sign problem for frustrated quantum systems. First, we assume that the wave function of the entire system is described as a direct products of local wave functions as in the MF approximation [Eq. (S1)], although the three-sublattice ansatz is not assumed. The total energy of the system is given by

$$E_{\text{cl}}(\{\mathbf{d}_i\}) = \langle \Psi^{\text{cl}} | \hat{\mathcal{H}} | \Psi^{\text{cl}} \rangle = J \sum_{\langle i,j \rangle} \left(|\mathbf{d}_i^* \cdot \mathbf{d}_j|^2 - \frac{1}{3} \right) - H \sum_i (|d_{i,1}|^2 - |d_{i,-1}|^2) \quad (\text{S3})$$

within the direct-product approximation. We first set the initial values of \mathbf{d}_i on the entire lattice sites to $L \times L$ complex random vectors distributed homogeneously on the sphere of radius one in 3 (real) + 3 (imaginary) dimensions. Starting with the initial state, we perform the standard Metropolis local updates of \mathbf{d}_i to generate a sequence of states weighted by the probability proportional to the Boltzmann factor $\exp(-E_{\text{cl}}(\{\mathbf{d}_i\})/k_B T)$. Typical simulations contain 10^5 and 2×10^6 Monte Carlo steps for the thermalization of the state and the samplings of physical quantities, respectively. One Monte Carlo step consists of one Metropolis sweep over all sites followed by two “relaxation acceleration” (RA) sweeps (which will be explained in Sec. C).

The quantum-mechanical expectation values of the local spin and quadrupolar moments can be calculated by

$$\lambda_i^A \equiv \langle \psi_i | \hat{\lambda}_i^A | \psi_i \rangle = \sum_{\sigma, \sigma'} \langle \sigma_i | \hat{\lambda}_i^A | \sigma'_i \rangle d_{i,\sigma}^* d_{i,\sigma'} \quad (\text{S4})$$

for a given site with vector \mathbf{d}_i . The eight components of the vector $\hat{\lambda}_i$ correspond to the spin components ($\hat{S}_i^x, \hat{S}_i^y, \hat{S}_i^z$) for $A = 1, 2, 3$ and quadrupolar components ($\hat{Q}_i^{x^2-y^2}, \hat{Q}_i^{z^2}, \hat{Q}_i^{xy}, \hat{Q}_i^{yz}, \hat{Q}_i^{xz}$) for $A = 4, 5, \dots, 8$, respectively, as in the

main text. To discuss the spontaneous symmetry breaking, we calculate the correlation lengths of the diagonal and transverse components:

$$\xi_{(1,2)}^{\parallel} = \frac{\sqrt{3}L}{4\pi} \sqrt{\frac{\mathcal{S}_{(1,2)}^{\parallel}(\mathbf{Q}_K)}{\mathcal{S}_{(1,2)}^{\parallel}(\mathbf{Q}_K + (0, 4\pi/\sqrt{3}L))} - 1} \quad \text{and} \quad \xi_{(1,2)}^{\perp} = \frac{\sqrt{3}L}{4\pi} \sqrt{\frac{\mathcal{S}_{(1,2)}^{\perp}(\mathbf{Q}_K)}{\mathcal{S}_{(1,2)}^{\perp}(\mathbf{Q}_K + (0, 4\pi/\sqrt{3}L))} - 1} \quad (\text{S5})$$

with the structure factors

$$\begin{aligned} \mathcal{S}_{(1)}^{\parallel}(\mathbf{k}) &= \frac{1}{L^2} \sum_{i,j} \langle\langle S_i^z S_j^z \rangle\rangle_T e^{-i\mathbf{k}\cdot(\mathbf{r}_i - \mathbf{r}_j)}, \quad \mathcal{S}_{(2)}^{\parallel}(\mathbf{k}) = \frac{1}{L^2} \sum_{i,j} \langle\langle Q_i^{z^2} Q_j^{z^2} \rangle\rangle_T e^{-i\mathbf{k}\cdot(\mathbf{r}_i - \mathbf{r}_j)}, \\ \mathcal{S}_{(1)}^{\perp}(\mathbf{k}) &= \frac{1}{L^2} \sum_{i,j} \frac{\langle\langle Q_i^{x^2-y^2} Q_j^{x^2-y^2} + Q_i^{xy} Q_j^{xy} \rangle\rangle_T}{2} e^{-i\mathbf{k}\cdot(\mathbf{r}_i - \mathbf{r}_j)}, \quad \text{and} \\ \mathcal{S}_{(2)}^{\perp}(\mathbf{k}) &= \frac{1}{L^2} \sum_{i,j} \frac{\langle\langle S_i^x S_j^x + S_i^y S_j^y + Q_i^{yz} Q_j^{yz} + Q_i^{xz} Q_j^{xz} \rangle\rangle_T}{2} e^{-i\mathbf{k}\cdot(\mathbf{r}_i - \mathbf{r}_j)}. \end{aligned} \quad (\text{S6})$$

Here, $\langle\langle \cdots \rangle\rangle_T$ means the thermal average in terms of Monte Carlo samplings and the ordering vector $\mathbf{k} = \mathbf{Q}_K \equiv (4\pi/3, 0)$ corresponds to the three-sublattice order shown as the inset of Fig. 2(a).

The stiffness $\rho_{S^z}(T)$ for a twist generated by the unitary transformation, $\hat{U}_{S^z}(q) \equiv \exp[iq \sum_i x_i \hat{S}_i^z]$, is defined in the standard way as the second derivative of the free energy per unit area with respect to the twist angle q :

$$\begin{aligned} \rho_{S^z}(T) &= \frac{1}{L^2 \Delta S} \left\langle \left. \frac{\partial^2 \langle \hat{U}_{S^z}(q) \hat{\mathcal{H}} \hat{U}_{S^z}^\dagger(q) \rangle}{\partial q^2} \right|_{q=0} \right\rangle_T - \frac{1}{k_B T} \left\langle \left(\left. \frac{\partial \langle \hat{U}_{S^z}(q) \hat{\mathcal{H}} \hat{U}_{S^z}^\dagger(q) \rangle}{\partial q} \right|_{q=0} \right)^2 \right\rangle_T \\ &= -\frac{2}{\sqrt{3}L^2} \left\langle \left. \frac{J}{2} \sum_{\langle i,j \rangle} (x_i - x_j)^2 \left(S_i^x S_j^x + S_i^y S_j^y + 4(Q_i^{x^2-y^2} Q_j^{x^2-y^2} + Q_i^{xy} Q_j^{xy}) + Q_i^{yz} Q_j^{yz} + Q_i^{xz} Q_j^{xz} \right) \right|_{q=0} \right\rangle_T \\ &\quad - \frac{2}{\sqrt{3}L^2 k_B T} \left\langle \left[\left. \frac{J}{2} \sum_{\langle i,j \rangle} (x_i - x_j) \left(S_i^x S_j^y - S_i^y S_j^x + 2(Q_i^{x^2-y^2} Q_j^{xy} - Q_i^{xy} Q_j^{x^2-y^2}) - (Q_i^{yz} Q_j^{xz} - Q_i^{xz} Q_j^{yz}) \right) \right|_{q=0} \right]^2 \right\rangle_T, \end{aligned} \quad (\text{S7})$$

where $\Delta S = \sqrt{3}/2$ is the area per site. Here, we choose the twist direction to be parallel to the x -axis, although the value of $\rho_{S^z}(T)$ does not depend on this choice for $L \rightarrow \infty$. In a similar way, the stiffness $\rho_{P_+^z}(T)$ regarding $\hat{U}_{P_+^z}(q) \equiv \exp[iq \sum_i x_i \hat{P}_{+,i}^z]$ with $\hat{P}_{+,i}^z \equiv \frac{1}{2} \hat{S}_i^z + \frac{\sqrt{3}}{2} \hat{Q}_i^{z^2}$ is defined as

$$\begin{aligned} \rho_{P_+^z}(T) &= -\frac{2}{\sqrt{3}L^2} \left\langle \left. \frac{J}{2} \sum_{\langle i,j \rangle} (x_i - x_j)^2 \left(4(P_{+,i}^x P_{+,j}^x + P_{+,i}^y P_{+,j}^y) + P_{-,i}^x P_{-,j}^x + P_{-,i}^y P_{-,j}^y + Q_i^{x^2-y^2} Q_j^{x^2-y^2} + Q_i^{xy} Q_j^{xy} \right) \right|_{q=0} \right\rangle_T \\ &\quad - \frac{2}{\sqrt{3}L^2 k_B T} \left\langle \left[\left. \frac{J}{2} \sum_{\langle i,j \rangle} (x_i - x_j) \left(2(P_{+,i}^x P_{+,j}^y - P_{+,i}^y P_{+,j}^x) - (P_{-,i}^x P_{-,j}^y - P_{-,i}^y P_{-,j}^x) + Q_i^{x^2-y^2} Q_j^{xy} - Q_i^{xy} Q_j^{x^2-y^2} \right) \right|_{q=0} \right]^2 \right\rangle_T, \end{aligned} \quad (\text{S8})$$

where $\hat{P}_{\pm}^x \equiv (\hat{S}^x \pm \hat{Q}^{xz})/\sqrt{2}$ and $\hat{P}_{\pm}^y \equiv (\hat{S}^y \pm \hat{Q}^{yz})/\sqrt{2}$.

Numetical data of the sMC simulations

Here we present some numerical data for the standard scaling analyses performed to determine the phase boundaries of Fig. 3 of the main text. All the three (LF, IF, and HF) phases possess a three-sublattice order in the diagonal

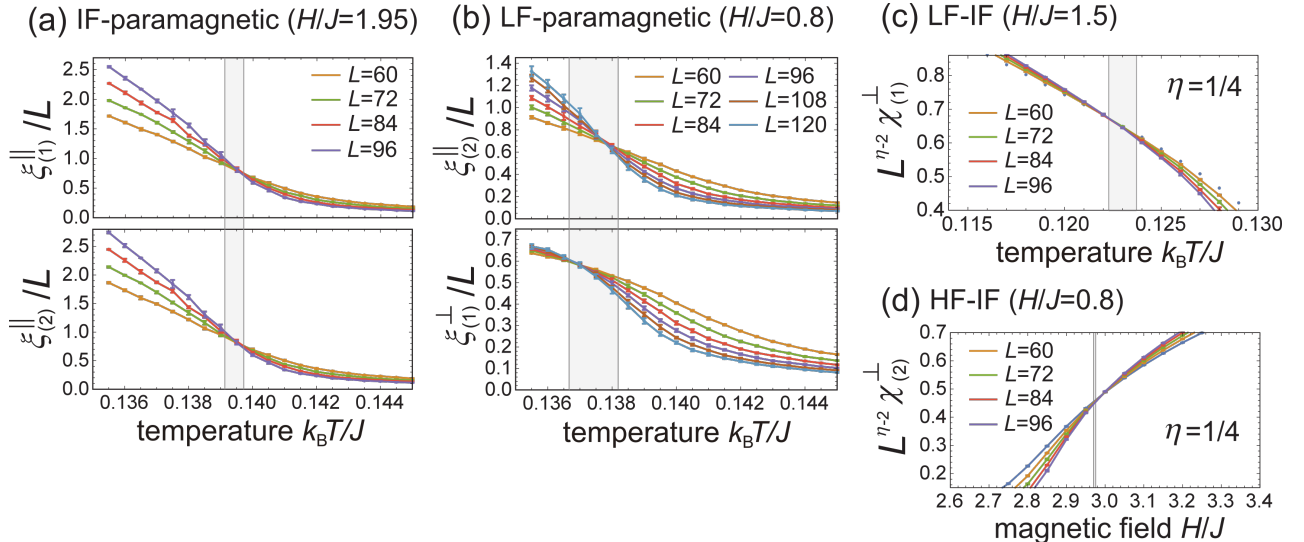


FIG. S1: Typical examples of the numerical data for the scaling analyses that determine the finite-temperature phase diagram shown in Fig. 3 of the main text. The error bars assigned to each data point are estimated as the square root of variance of about 10 independent sMC simulations. The shaded bands indicate the estimated transition points with their error bar.

components, S^z and Q^{z^2} . Therefore, the transition points to the paramagnetic phase can be identified by the divergence of $\xi_{(1,2)}^{\parallel}$. Figure S1 (a) shows a typical example of the transition from the IF to paramagnetic phase. The curves of the scaled correlation length $\xi_{(1,2)}^{\parallel}/L$ for different linear sizes L cross each other at a critical point, within the error bar estimated from the square root of the variance over about 10 sMC simulations. We plot in Fig. 3 the crossing points in $\xi_{(2)}^{\parallel}/L$, which are slightly less size-dependent, as the phase boundary from the ordered to the paramagnetic states.

Note that, in the standard Kosterlitz-Thouless transition of the 2D XY model with rotational symmetry, the scaled correlation length of the transverse (XY) components does not exhibit an isolated critical (crossing) point but a finite critical range from $T = 0$ with a constant value independent of L . Interestingly, the scaled correlation length of the transverse components, $\xi_{(1)}^{\perp}/L$ ($\xi_{(2)}^{\perp}/L$) in the present case shows a crossing behavior in the vicinity of the transitions from the LF (HF) to paramagnetic transitions, in spite of the continuous nature of the rotational symmetries of the system around the S^z and Q^{z^2} axes [see an example for the LF-paramagnetic transition in Fig. S1(b)]. This may be attributed to the combined effect of the simultaneous discrete (diagonal) and continuous (transverse) symmetry breakings. A similar (apparent) crossing behavior of the scaled correlation length for the transverse components has been reported in previous studies on some related 2D models with combined discrete and continuous symmetry breakings [2]. The crossing points in the scaled correlation lengths of the diagonal and transverse components are located at almost the same position (within the error bar) as seen in Fig. 3 of the main text.

From the LF to the IF (HF to IF) phase, the topological transition associated with the unbinding of pairs of half-vortex and half-antivortex in the plane of $Q^{x^2-y^2}$ and Q^{xy} (P_+^x and P_+^y) occurs, as explained in the main text. In this case, the corresponding scaled correlation length does not exhibit an isolated critical point. Therefore, to locate the topological transition points, we perform the scaling analysis on the susceptibilities of the corresponding quantities:

$$\chi_{(1)}^{\perp} = \frac{J}{k_B T} \mathcal{S}_{(1)}^{\perp}(\mathbf{Q}_K) \quad \text{and} \quad \chi_{(2)}^{\perp} = \frac{J}{k_B T} \mathcal{S}_{(2)}^{\perp}(\mathbf{Q}_K), \quad (\text{S9})$$

which obey the following scaling relations:

$$\chi_{(1,2)}^{\perp} = L^{2-\eta} \tilde{\chi}_{(1,2)}^{\perp}(t L^{1/\nu}) \quad (\text{S10})$$

with unknown universal functions $\tilde{\chi}_{(1,2)}^{\perp}$ of $t = (T - T_c)/T_c$. Here, η and ν are the correlation function and correlation length critical exponents, respectively. At the LF-to-IF (HF-to-IF) topological phase transition, $\chi_{(1)}^{\perp}$ ($\chi_{(2)}^{\perp}$) is expected to scale with the exact Kosterlitz-Thouless exponent $\eta = 1/4$ [3]. According to Eq. (S10), the quantities $L^{\eta-2} \chi_{(1,2)}^{\perp}$ become size-independent at the corresponding transition points $t = 0$ with $\eta = 1/4$. Figure S1(c) and S1(d) show

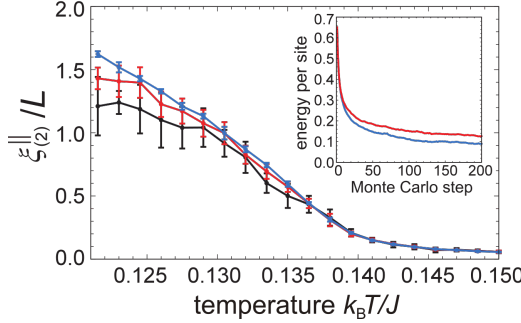


FIG. S2: Comparison of the results with and without RA. The values of the scaled correlation length $\xi_{(2)}^{\parallel}/L$ for $H/J = 0.5$ and $L = 96$ obtained by the sMC simulations (i) for 10^6 samples without RA (black), (ii) for 3×10^6 samples without RA (red), and (iii) for 10^6 samples with RA (blue) are plotted. The error bars are estimated from the square root of the variance over nine independent sMC simulations. The inset shows the energy of the system per site for the first 200 Monte Carlo steps in the thermalization processes with (blue) and without (red) RA.

typical examples of the scaling analysis performed to determine the LF-IF and HF-IF boundaries, respectively, plotted in Fig. 3.

Relaxation acceleration techniques

Technical details of the “relaxation acceleration” (RA) techniques we introduced in the main text are presented below. The explicit form of the local effective Hamiltonian on site i within the direct-product approximation is given by

$$\hat{\mathcal{H}}_i^{\text{loc}} \equiv (\otimes_{j \neq i} \langle \psi_j |) \hat{\mathcal{H}} (\otimes_{j \neq i} | \psi_j \rangle) = \frac{J}{2} \sum_{j \in \text{NN}_i} \left(\mathbf{S}_j \cdot \hat{\mathbf{S}}_i + \mathbf{Q}_j \cdot \hat{\mathbf{Q}}_i \right) - H \hat{S}_i^z, \quad (\text{S11})$$

where the sum $\sum_{j \in \text{NN}_i}$ runs over all nearest-neighbor sites of site i and the terms independent on the local state on site i are ignored. Note that the energy of the system within the direct-product approximation [Eq. (S3)] is preserved under the local unitary transformation $e^{ic\hat{\mathcal{H}}_i^{\text{loc}}} |\psi_i\rangle$ with c being a real number. Using the local unitary transformations combined with the Metropolis updates, one can avoid the problem of trapping into local minima and significantly improve the decorrelation between the adjacent Monte-Carlo samples in the Markov chain. The operator $e^{ic\hat{\mathcal{H}}_i^{\text{loc}}}$ can be described as the matrix exponential of a 3×3 matrix on the local state basis (S1). The numerical cost for computing the matrix exponential can be reduced by using the spectral decomposition and the analytical form of the eigenvalues of the 3×3 Hermitian matrix $\hat{\mathcal{H}}_i^{\text{loc}}$ [4].

In Fig. S2, we compare the calculated values of the scaled correlation length $\xi_{(2)}^{\parallel}/L$ for $H/J = 0.5$ and $L = 96$, as an example, obtained by the sMC simulations (i) for 10^6 samples without RA (black), (ii) for 3×10^6 samples without RA (red), and (iii) for 10^6 samples with RA (blue). Here, one Monte-Carlo step consists of two sweeps of the RA operations over all sites following one Metropolis update sweep, and the sampling of the physical quantities for calculating the thermal average is performed at every Monte-Carlo step. The arbitrary real number c is chosen to be uniformly distributed random numbers in $[-\pi f_n, \pi f_n]$ with f_n being the Frobenius norm of the matrix form of $\hat{\mathcal{H}}_i^{\text{loc}}$. As can be seen in Fig. S2, the error bars of the data are clearly diminished owing to the RA operations, even in comparison of (ii) and (iii) with a three times difference in those sample numbers, which take roughly same computation time. This indicates the reduction of the autocorrelation between the samples. The inset shows the sMC thermalization processes from an initial state with uniformly distributed random vectors \mathbf{d}_i on the entire lattice sites. It can be seen that the case with RA shows faster convergence to the thermal equilibrium.

[1] E. M. Stoudenmire, S. Trebst, and L. Balents, Phys. Rev. B **79**, 214436 (2009).
[2] L. Seabra, T. Momoi, P. Sindzingre, and N. Shannon, Phys. Rev. B **84**, 214418 (2011).
[3] M. V. Gvozdikova, P.-E. Melchy, M. E. Zhitomirsky, J. Phys.: Condens. Matter **23**, 164209 (2011).

[4] J. Copp, Int. J. Mod. Phys. **C19**, 523 (2008).